J. Fluid Mech. (2009), *vol.* 631, *pp.* 127–148.
doi:10.1017/S0022112009006806 Printed in the United Kingdom

Swimming due to transverse shape deformations

EVA KANSO†

Aerospace and Mechanical Engineering, University of Southern California
854 Downey Way, Los Angeles, CA 90089-1191, USA

(Received 9 March 2008 and in revised form 24 February 2009)

Balance laws are derived for the swimming of a deformable body due to prescribed shape changes and the effect of the wake vorticity. The underlying balances of momenta, though classical in nature, provide a unifying framework for the swimming of three-dimensional and planar bodies and they hold even in the presence of viscosity. The derived equations are consistent with Lighthill's reactive force theory for the swimming of slender bodies and, when neglecting vorticity, reduce to the model developed in Kanso *et al.* (*J. Nonlinear Sci.*, vol. 15, 2005, p. 255) for swimming in potential flow. The locomotion of a deformable body is examined through two sets of examples: the first set studies the effect of cyclic shape deformations, both flapping and undulatory, on the locomotion in potential flow while the second examines the effect of the wake vorticity on the net locomotion. In the latter, the vortex wake is modelled using pairs of point vortices shed periodically from the tail of the deformable body.

1. Introduction

The net locomotion of a deformable body submerged in an infinite volume of fluid depends critically on the dynamic coupling between the prescribed shape deformations and the unsteady motion of the surrounding fluid. A mathematical description of this coupling at finite Reynolds numbers would require taking into account the detailed effects of viscosity which are primarily manifested in the dynamics of the thin shear layers around the body. These layers remain attached over parts of the body and separate at the body tail (or fins when accounted for in the model) to create vortical structures whose subsequent dynamics is also influenced by viscosity. Mid-body separation and vortex shedding have also been reported (see, e.g. Zhu *et al.* 2002).

For swimming at large Reynolds numbers due to transverse shape deformations (e.g. Carangiform and Thunniform swimming), the viscous effects may be modelled using a purely inviscid theory (see Wu 1961, 1971*a*; Katz & Weihs 1978, 1979; Jones 2003; Shukla & Eldredge 2007). Separation, vortex shedding and vortex wakes can be modelled by imposing an unsteady Kutta condition and including a vortex sheet, that is, a surface across which the tangential component of the fluid velocity is discontinuous but the normal component is continuous, originating from the tail of the waving body. The Kutta condition requires the velocity and pressure to be continuous and bounded at the trailing edge. The problem of resolving the vortex shedding and vortex sheet dynamics for large shape deformations is quite challenging even for prescribed swimming motions of the solid body (see Jones 2003; Shukla & Eldredge 2007).

† Email address for correspondence: kanso@usc.edu

In the classical work of Wu on the swimming of a planar (infinite depth) deformable plate, the author used the assumption of small shape amplitudes which enables one to solve for the trailing vortex sheet analytically and investigate the problem of optimum shape deformations in the sense of minimizing the energy lost in creating the trailing wake (see Wu 1961, 1971*a*, *b*). Lighthill, on the other hand, studied the swimming of a slender body due to large amplitude deformations (see, e.g. Lighthill 1975) and avoided solving for the complex wake dynamics by considering the momentum balance in a control volume containing the deformable body and bounded by a plane attached at its trailing edge. The studies of both Lighthill and Wu focused mainly on the swimming at constant velocity with the efficiency of long range cruising in mind. Later, Weihs (1972, 1973) modified Lighthill's slender body theory for applications to turning as well as sudden starting/stopping maneuvers.

One of the main objectives of this paper is to derive balance laws for the swimming of a deformable body in an inviscid fluid in response to prescribed (actively controlled) shape deformations and the effect of the wake vorticity. The underlying balances of momenta, though classical in nature, provide a unifying framework for the swimming of three-dimensional and planar bodies and they may hold even in the presence of viscosity – a fact often overlooked in the literature on swimming. The derived equations, when applied to the swimming of slender bodies, can be viewed as a generalization of Lighthill's 'reactive' force theory. When neglecting vorticity, that is, for swimming in potential flow, the derived equations reduce to the model developed in Kanso *et al.* (2005) for the motion of an articulated body in irrotational flow. This is not a coincidence. In fact, in his analysis of the swimming of an elongated fish (slender body) at large Reynolds numbers, Lighthill argues that the added or virtual mass of fluid which acquires momentum through shape changes of the animal far exceeds the associated animal's mass and the 'resistive' forces due to boundary layer and vortex shedding. That is, the 'reactive' forces (proportional to the added mass) play a central role in the locomotion of these animals. It is exactly this added mass effect that we capture in the potential flow models. Note that an algorithm that isolates the reactive forces in the swimming at the finite Reynolds numbers can be found in Eldredge (2008).

The derived equations are used to study the effect of cyclic shape changes on the locomotion of a deformable body in potential flow due to the added mass effect (no wake). This study differs from the one discussed in Kanso *et al.* (2005) in which it considers the swimming of an elastic body as opposed to a system of connected rigid bodies. This allows one to examine both undulatory and flapping deformations. Indeed, we prescribe both types of deformations: undulations of the centreline, i.e. smooth travelling waves similar to those considered in Wu (1961), and flapping, or piecewise smooth waves of linear form, similar to those considered in Kanso *et al.* (2005). Gaits due to such shape changes are numerically simulated using a panel method (see, e.g. Katz & Plotkin 2001) and their locomotion properties are compared. In particular, for the flapping deformations, we identify optimal shape trajectories for which the deformable body achieves maximum displacement and, for the undulatory deformations, we examine the effect of the wavelength of the travelling waves on the net displacement.

One of the advantages of the derived balance laws is that they do not impose a specific approach for modelling the wake. When fast calculations are a priority, say, when using the model for an online controller on a robotic fish, the wake can be approximated using classical methods of unsteady aerodynamics in terms of pretabulated lift and drag coefficients (as done in Weihs 1972, 1973) or can be

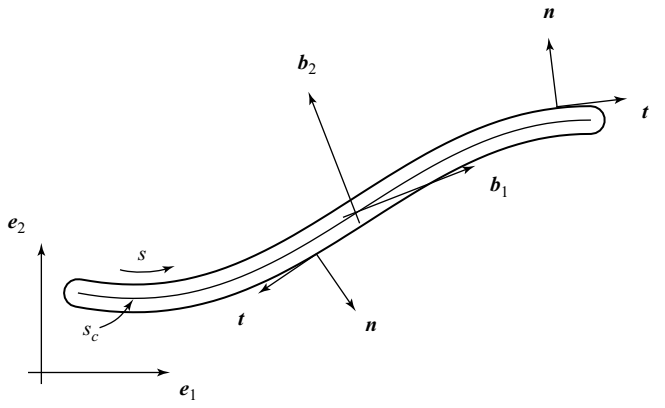

FIGURE 1. A deformable body $\mathscr{B}$ immersed in an infinitely large volume $\mathscr{F}$ of an inviscid and incompressible fluid which is at rest at infinity and undergoing prescribed planar shape deformations.

computed using a surrogate wake of discrete vortex structures (point vortices or vortex rings as those employed in Shashikanth *et al.* 2002, 2008; Borisov & Mamaev 2003; Kanso & Oskouei 2008; Shashikanth 2006). We follow this approach for studying the effect of the wake vorticity on the net locomotion. Namely, we model the wake using pairs of point vortices shed periodically from the tail of the deformable body. If a more accurate description of the wake is necessary, the shed vorticity can be obtained by coupling the derived equations to a numerical solver that accurately computes the wake vorticity (as done in Jones 2003; Shukla & Eldredge 2007 within the perfect fluid theory or using a numerical solver that accounts for viscosity as in Peskin 2002; Eldredge 2008). These directions will be pursued in future works.

The organization of this paper is as follows: The problem setting is described in § 2. The balance laws governing the locomotion of a deformable body due to prescribed shape changes are derived in § 3. A discussion of the energy transfer during the swimming process is presented in § 4. The equations governing the motion of a deformable body in potential flow are derived in § 5. Several examples of swimming in potential flow are presented in § 6 while swimming due to dipole shedding is discussed in § 7. The findings of this work are summarized in § 8. In the Appendix, we tie the balance laws derived in § 3 to Lighthill's slender body theory.

2. Setting

Consider a planar (infinite depth) deformable body $\mathscr{B}$ immersed in an infinitely large volume $\mathscr{F}$ of an inviscid and incompressible fluid which is at rest at infinity; a two-dimensional cross-section of the body is shown in figure 1. Let the body undergo prescribed two-dimensional shape deformations, not necessarily small, of the general form

$$\boldsymbol{x}_{shape} = x_{shape}(s,t)\,\boldsymbol{e}_1 + y_{shape}(s,t)\,\boldsymbol{e}_2, \tag{2.1}$$

where x_{shape} and y_{shape} are functions of the arclength s along the boundary $\partial\mathscr{B}$ of a cross-section of the body and time t. The functions x_{shape} and y_{shape} are expressed with respect to an orthonormal inertial frame $\{\boldsymbol{e}_{1,2,3}\}$ where $\{\boldsymbol{e}_1, \boldsymbol{e}_2\}$ span the plane of deformations and $\boldsymbol{e}_3$ is the unit normal to this plane. The shape deformations satisfy

the inextensibility condition

$$\left(\frac{\partial x_c}{\partial s_c}\right)^2 + \left(\frac{\partial y_c}{\partial s_c}\right)^2 = 1, \tag{2.2}$$

where x_c and y_c denote coordinates of the centreline and s_c is the arclength along the centreline. Also, let shape deformations satisfy the area-preservation condition,

$$\text{Area} = \frac{1}{2}\int_{\partial\mathscr{B}} \left(x_{shape}\frac{\partial y_{shape}}{\partial s} - y_{shape}\frac{\partial x_{shape}}{\partial s}\right) \mathrm{d}s = \text{constant for all time } t. \tag{2.3}$$

The shape velocity can be expressed as follows:

$$\boldsymbol{v}_{shape} = \frac{\partial x_{shape}}{\partial t}\,\boldsymbol{e}_1 + \frac{\partial y_{shape}}{\partial t}\boldsymbol{e}_2, \tag{2.4}$$

or, equivalently,

$$\boldsymbol{v}_{shape} = \left(\frac{\partial x_{shape}}{\partial t}\frac{\partial x_{shape}}{\partial s} + \frac{\partial y_{shape}}{\partial t}\frac{\partial y_{shape}}{\partial s}\right)\boldsymbol{t} + \left(\frac{\partial y_{shape}}{\partial t}\frac{\partial x_{shape}}{\partial s} - \frac{\partial x_{shape}}{\partial t}\frac{\partial y_{shape}}{\partial s}\right)\boldsymbol{n}. \tag{2.5}$$

Here, $(\boldsymbol{t}, \boldsymbol{n})$ are the tangential and normal unit vectors to $\partial\mathscr{B}$ with $\boldsymbol{n}$ pointing towards the fluid and are related to $(\boldsymbol{e}_1, \boldsymbol{e}_2)$ by

$$\boldsymbol{t} = \frac{\partial x_{shape}}{\partial s}\boldsymbol{e}_1 + \frac{\partial y_{shape}}{\partial s}\boldsymbol{e}_2, \qquad \boldsymbol{n} = -\frac{\partial y_{shape}}{\partial s}\boldsymbol{e}_1 + \frac{\partial x_{shape}}{\partial s}\boldsymbol{e}_2. \tag{2.6}$$

This transformation is invertible as long as the boundary deformations are not degenerate – a condition assumed to hold here. Note that in the presence of a sharp edge, this transformation is valid everywhere except at the edge where $\boldsymbol{t}$ and $\boldsymbol{n}$ are ill defined. One would need to consider an open neighbourhood of the sharp edge and decompose the boundary integrals that arise in § 3 into an integral over the smooth portion of the body and a second integral in the neighbourhood of the edge.

The net locomotion of the body $\mathscr{B}$ is identified with a rotation β about $\boldsymbol{e}_3$ and a translation (x_o, y_o) in the $\{\boldsymbol{e}_1, \boldsymbol{e}_2\}$ directions, say of the geometric centre of $\mathscr{B}$. The angular and translational velocities can be expressed in the fixed inertial frame as $\dot{\beta}\,\boldsymbol{e}_3$ and $\boldsymbol{v} = \dot{x}_o\boldsymbol{e}_1 + \dot{y}_o\boldsymbol{e}_2$ (the dot is used to denote the partial derivative with respect to time, $\partial/\partial t$).

It is convenient for the development in § 5 to introduce body-fixed coordinates $\boldsymbol{X}$ which are measured from the body-fixed orthonormal frame $\{\boldsymbol{b}_{1,2,3}\}$ whose origin is placed at the geometric centre $\boldsymbol{x}_o$. The axes $\{\boldsymbol{b}_{1,2,3}\}$ are related to $\{\boldsymbol{e}_{1,2,3}\}$ via the proper-orthogonal tensor $\boldsymbol{R}$,

$$\begin{pmatrix}\boldsymbol{e}_1\\ \boldsymbol{e}_2\\ \boldsymbol{e}_3\end{pmatrix} = \underbrace{\begin{pmatrix}\cos\beta & -\sin\beta & 0\\ \sin\beta & \cos\beta & 0\\ 0 & 0 & 1\end{pmatrix}}_{(R)} \begin{pmatrix}\boldsymbol{b}_1\\ \boldsymbol{b}_2\\ \boldsymbol{b}_3\end{pmatrix}. \tag{2.7}$$

The point transformation from the body to the inertial frame can be represented as

$$\boldsymbol{x} = \boldsymbol{R}\boldsymbol{X} + \boldsymbol{x}_o, \tag{2.8}$$

where $\boldsymbol{x} = x\,\boldsymbol{e}_1 + y\,\boldsymbol{e}_2$ and $\boldsymbol{X} = X\,\boldsymbol{b}_1 + Y\,\boldsymbol{b}_2$, while vectors transform as $\boldsymbol{v} = \boldsymbol{R}\boldsymbol{V}$. The angular and translational velocities expressed in the body frame take the form $\boldsymbol{\Omega} = \Omega\,\boldsymbol{b}_3$ (where $\Omega = \dot{\beta}$) and $\boldsymbol{V} = V_1\boldsymbol{b}_1 + V_2\boldsymbol{b}_2$ (where $V_1 = \dot{x}_o\cos\beta + \dot{y}_o\sin\beta$ and $V_2 = -\dot{x}_o\sin\beta + \dot{y}_o\cos\beta$). One could also prescribe the shape deformations with

respect to the body-fixed frame as $\boldsymbol{X}_{shape} = X_{shape}(s,t)\boldsymbol{b}_1 + Y_{shape}(s,t)\boldsymbol{b}_2$, and write the shape velocity $\boldsymbol{V}_{shape}(= \boldsymbol{R}^{\mathrm{T}}\boldsymbol{v}_{shape})$ in body frame. The symbol $()^{\mathrm{T}}$ denotes the transpose operation.

3. Momentum balance

The balance laws are derived based on the following assumptions:

(i) There are no external forces or moments applied on the solid–fluid system.

(ii) The body is massless and the fluid density is normalized to unity.

(iii) The body at all times can maintain its instantaneous shape under the hydrodynamic pressure loading on its boundary. That is, the net dynamic effect (if any) of the pressure field on the boundary is always a locomotion (recoil effects are not accounted for).

(iv) All vorticity in the fluid is confined to the trailing wake. Moreover, vorticity in the far wake is assumed to decay rapidly enough to ensure convergence of integrals of vorticity over the infinite fluid domain that may arise.

For planar (two-dimensional) bodies, the balance of linear momentum, or more precisely impulse, of the body–fluid system reads as (see Saffman 1992)

$$\frac{\mathrm{d}}{\mathrm{d}t}\left[\oint_{\partial\mathscr{B}} \boldsymbol{x}\times(\boldsymbol{n}\times\boldsymbol{u})\,\mathrm{d}s + \int_{\mathscr{F}} \boldsymbol{x}\times\boldsymbol{\omega}\,\mathrm{d}a\right] = 0, \tag{3.1}$$

where $\boldsymbol{x}$ denotes the position vector with respect to the inertial frame, $\boldsymbol{u}$ denotes the spatial velocity field of the fluid, $\boldsymbol{\omega} = \nabla\times\boldsymbol{u}$ is the vorticity of the fluid, $\mathrm{d}a$ and $\mathrm{d}s$ are standard area and line elements. Similarly, the balance of angular momentum or impulse about the origin of the inertial frame takes the form

$$\frac{\mathrm{d}}{\mathrm{d}t}\left[-\frac{1}{2}\oint_{\partial\mathscr{B}} \|\boldsymbol{x}\|^2(\boldsymbol{n}\times\boldsymbol{u})\,\mathrm{d}s - \frac{1}{2}\int_{\mathscr{F}} \|\boldsymbol{x}\|^2\boldsymbol{\omega}\,\mathrm{d}a\right] = 0. \tag{3.2}$$

The momentum balance laws (3.1)–(3.2) hold in general even in the presence of viscosity. It is worth noting that, in unbounded two-dimensional flows, the balance of linear momentum remains true in the presence of viscosity while that of angular momentum is true only when there is no net circulatory flow at infinity (see Saffman 1992, §§ 3.6 and 3.10). In this work, we consider an inviscid and incompressible fluid. The fluid velocity $\boldsymbol{u}$ can be written using the Helmholtz–Hodge decomposition as follows:

$$\boldsymbol{u} = \nabla\phi + \boldsymbol{u}_w = \nabla\phi + \nabla\times\boldsymbol{\psi}. \tag{3.3}$$

where $\boldsymbol{u}_w = \nabla\times\boldsymbol{\psi}$. The vector potential $\boldsymbol{\psi}$ satisfies $\Delta\boldsymbol{\psi} = -\boldsymbol{\omega}$ subject to the boundary conditions $(\nabla\times\boldsymbol{\psi})\cdot\boldsymbol{n} = 0$ on $\partial\mathscr{B}$ and $\nabla\times\boldsymbol{\psi} = 0$ at infinity ($\boldsymbol{\psi}$ is zero in the absence of vorticity around the body). The potential function ϕ is harmonic, that is, it is the solution to Laplace's equation $\Delta\phi = 0$, subject to impermeable boundary conditions on $\partial\mathscr{B}$ ($\nabla\phi\cdot\boldsymbol{n}$ = normal velocity of the boundary) and the velocity is required to vanish at infinity. Namely, one has

$$\frac{\partial\phi}{\partial n} = (\boldsymbol{v}_{shape} + \boldsymbol{v} + \dot{\beta}\,\boldsymbol{e}_3\times\boldsymbol{x})\cdot\boldsymbol{n} \quad \text{on } \partial\mathscr{B}, \qquad \nabla\phi = 0 \quad \text{at } \infty. \tag{3.4}$$

Boundary conditions (3.4) are a result of the inviscid fluid assumption. By linearity of Laplace's equation, one can write, following Kirchhoff (see Lamb 1932),

$$\phi = \dot{\beta}\varphi_\beta + \dot{x}_o\varphi_x + \dot{y}_o\varphi_y + \varphi_{shape}, \tag{3.5}$$

where $\varphi_\beta, \varphi_x, \varphi_y$ are called velocity potentials and are solutions to Laplace's equation subject to

$$\frac{\partial \varphi_\beta}{\partial n} = \boldsymbol{x} \times \boldsymbol{n} \cdot \boldsymbol{e}_3 \ , \quad \frac{\partial \varphi_x}{\partial n} = \boldsymbol{n} \cdot \boldsymbol{e}_1 \ , \quad \frac{\partial \varphi_y}{\partial n} = \boldsymbol{n} \cdot \boldsymbol{e}_2 \quad \text{on } \partial\mathscr{B}. \tag{3.6}$$

The function φ_{shape} is also harmonic ($\Delta\varphi_{shape} = 0$) and satisfies $\nabla\varphi_{shape} \cdot \boldsymbol{n} = \boldsymbol{v}_{shape} \cdot \boldsymbol{n}$ on $\partial\mathscr{B}$. That is, φ_{shape} is the potential function associated with the shape deformations only. Clearly, φ_β, φ_x, φ_y and φ_{shape} all depend on the instantaneous shape of $\mathscr{B}$.

One can readily verify, on substituting (3.5) into (3.3), employing the resulting expression for $\boldsymbol{u}$ in (3.1) and (3.2) and using standard vector identities and the divergence theorem, that (3.1) and (3.2) can be rewritten in the convenient form

$$\boldsymbol{F} = -\frac{\mathrm{d}\boldsymbol{p}_{shape}}{\mathrm{d}t} - \boldsymbol{F}_w, \quad \boldsymbol{M} = -\frac{\mathrm{d}\pi_{shape}}{\mathrm{d}t} - \boldsymbol{M}_w, \tag{3.7}$$

where $\boldsymbol{F}$ and $\boldsymbol{M}$ are the reactive forces and moments with which the fluid acts on the deformable body to cause it to achieve a net locomotion,

$$\begin{aligned} \boldsymbol{F} &= \frac{\mathrm{d}\boldsymbol{p}_{loc}}{\mathrm{d}t} + \frac{\mathrm{d}}{\mathrm{d}t} \oint_{\partial\mathscr{B}} \boldsymbol{x} \times (\boldsymbol{n} \times \boldsymbol{u}_w)\, \mathrm{d}s, \\ \boldsymbol{M} &= \frac{\mathrm{d}\pi_{loc}}{\mathrm{d}t} - \frac{\mathrm{d}}{\mathrm{d}t} \left[\frac{1}{2} \oint_{\partial\mathscr{B}} \|\boldsymbol{x}\|^2 (\boldsymbol{n} \times \boldsymbol{u}_w)\, \mathrm{d}s \right], \end{aligned} \tag{3.8}$$

with

$$\boldsymbol{p}_{loc} = \oint_{\partial\mathscr{B}} (\dot\beta\varphi_\beta + \dot x_o \varphi_x + \dot y_o \varphi_y)\boldsymbol{n}\ \mathrm{d}s, \quad \pi_{loc} = \oint_{\partial\mathscr{B}} (\dot\beta\varphi_\beta + \dot x_o \varphi_x + \dot y_o \varphi_y)\boldsymbol{x} \times \boldsymbol{n}\ \mathrm{d}s. \tag{3.9}$$

In (3.7), $\boldsymbol{p}_{shape}$ and π_{shape} are the linear and angular momenta imparted to the fluid due to shape changes,

$$\boldsymbol{p}_{shape} = \oint_{\partial\mathscr{B}} \varphi_{shape} \boldsymbol{n}\ \mathrm{d}s, \quad \pi_{shape} = \oint_{\partial\mathscr{B}} \varphi_{shape}\, \boldsymbol{x} \times \boldsymbol{n}\ \mathrm{d}s. \tag{3.10}$$

Finally, $\boldsymbol{F}_w$ and $\boldsymbol{M}_w$ denote the rate of change of the linear and angular impulses of the wake (note that the impulse of the wake depends on both the vortex shedding and the wake motion),

$$\boldsymbol{F}_w = \frac{\mathrm{d}}{\mathrm{d}t} \int_{\mathscr{F}} \boldsymbol{x} \times \boldsymbol{\omega}\ \mathrm{d}a, \quad \boldsymbol{M}_w = \frac{\mathrm{d}}{\mathrm{d}t} \left[-\frac{1}{2} \int_{\mathscr{F}} \|\boldsymbol{x}\|^2 \boldsymbol{\omega}\ \mathrm{d}a \right]. \tag{3.11}$$

Equations (3.7) govern the motion of the deformable body due to prescribed shape changes and their interaction with the wake vorticity. The shape momenta $\boldsymbol{p}_s$ and π_s can be readily computed for a prescribed shape deformation. To close the model, one needs to compute $\boldsymbol{F}_w$ and $\boldsymbol{M}_w$, which represent the contribution of vortex shedding and wake vorticity to the momentum balance, as well as the terms involving the wake contribution to $\boldsymbol{F}$ and $\boldsymbol{M}$ in (3.8). This closure can be obtained in a variety of ways the simplest of which is to consider an irrotational (potential) fluid model. The effect of the fluid is then completely encoded using the added mass effect and the terms $\boldsymbol{F}_w$ and $\boldsymbol{M}_w$ are set to zero. This case is discussed in §§ 5 and 6. Another approach would be to model the wake using discrete vortex structures as done in Katz & Weihs (1978, 1979) for a flexible body or in Shashikanth *et al.* (2002) and Kanso & Oskouei (2008) for a rigid body interacting with point vortices. This approach is pursued in § 7. If a more accurate description of the wake is necessary, $\boldsymbol{F}_w$ and $\boldsymbol{M}_w$ can be computed by coupling (3.7) to a numerical solver that computes the shed vorticity either within the

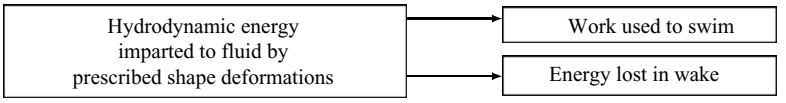

FIGURE 2. Energy transfer during the swimming process (adapted from Wu 1971*a*).

inviscid model as in Shukla & Eldredge (2007) or by using a numerical solver that accounts for viscosity as in Peskin (2002) or Eldredge (2008). These directions will be pursued in future studies.

We conclude this section by noting that (3.7) hold for a three-dimensional deformable body assumed to undergo planar locomotion due to planar shape deformations. Indeed, the kinematic description of the shape deformations in (2.1) and the inextensibility constraint (2.2) are equally applicable to a two-dimensional body as well as a three-dimensional body (not necessarily axisymmetric) undergoing planar deformations. That is, this kinematic description is valid for two-dimensional and three-dimensional flows. In three-dimensional, the arclength s parameterizes the cross-sectional boundary in the plane of motion. Of course, a second parameter in the transverse direction is needed to fully describe the surface boundary of the body. The area-preservation constraint (2.3) should be interpreted as a volume-preservation constraint and the boundary line integral should be replaced by a boundary surface integral. To arrive at (3.7), one follows a similar approach to the one presented above after writing the counterparts of (3.1) and (3.2) in three-dimensional. Namely, one starts by writing

$$\begin{aligned} \frac{\mathrm{d}}{\mathrm{d}t}\left[\oint_{\partial\mathscr{B}} \boldsymbol{x}\times(\boldsymbol{n}\times\boldsymbol{u})\,\mathrm{d}a+\frac{1}{2}\int_{\mathscr{F}}\boldsymbol{x}\times\boldsymbol{\omega}\,\mathrm{d}v\right]&=0,\\ \frac{\mathrm{d}}{\mathrm{d}t}\left[-\frac{1}{2}\oint_{\partial\mathscr{B}}\|\boldsymbol{x}\|^2(\boldsymbol{n}\times\boldsymbol{u})\,\mathrm{d}a-\frac{1}{2}\int_{\mathscr{F}}\|\boldsymbol{x}\|^2\boldsymbol{\omega}\,\mathrm{d}v\right]&=0. \end{aligned} \tag{3.12}$$

where $\mathrm{d}v$ and $\mathrm{d}a$ are standard volume and area elements. Note that (3.12) differ from (3.1) and (3.2) only by a factor of half in the linear impulse of the vorticity. The fact that this factor is missing in the two-dimensional equation can be traced to the vortex lines not being closed in two-dimensional flows. For more details (see Saffman 1992, chapter 3).

4. Energy consideration

From an energy perspective, the entire swimming process begins with the biochemical energy of the fish (or the chemical energy of a robotic swimmer) which is converted into mechanical energy for maintaining the body deformations. The mechanical energy is then transformed into hydrodynamic energy. Part of the hydrodynamic energy is spent in useful work, used to swim, and the remaining part is energy lost in the flow wake (see figure 2). Under the idealized conditions employed in this paper (no dissipation and negligible elastic effects), the mechanical energy necessary to maintain the shape deformations is equal to the hydrodynamic energy input into the fluid. The aim of this section is to discuss the transfer of hydrodynamic energy into work used to achieve a net locomotion.

We begin by computing the total kinetic energy of the fluid $T_{\mathscr{F}}$. The kinetic energy $T_{\mathscr{F}}$ is given in spatial representation by

$$T_{\mathscr{F}}=\frac{1}{2}\int_{\mathscr{F}}\|\boldsymbol{u}\|^2\,\mathrm{d}a=\frac{1}{2}\oint_{\partial\mathscr{B}}\phi\frac{\partial\phi}{\partial n}\,\mathrm{d}s+\frac{1}{2}\oint_{\partial\mathscr{B}}\boldsymbol{u}_w\times\boldsymbol{\psi}\,\mathrm{d}s+\frac{1}{2}\int_{\mathscr{F}}\boldsymbol{\psi}\cdot\boldsymbol{\omega}\,\mathrm{d}a. \tag{4.1}$$

The last term in (4.1) denotes the kinetic energy of the wake while the second last term represents the coupling between the body's motion and the wake. One can readily verify, writing ϕ as in (3.5) and following a standard procedure (see, e.g. Kanso *et al.* 2005), that the first term in the kinetic energy $T_{\mathscr{F}}$ can be rewritten as

$$\frac{1}{2}\oint_{\partial\mathscr{B}} \phi \frac{\partial \phi}{\partial n}\, \mathrm{d}s = T_{loc} + T_{couple} + T_{shape}. \tag{4.2}$$

In (4.2), one has

$$\begin{gathered} T_{loc} = \frac{1}{2}(\boldsymbol{\Omega}\cdot\pi_{loc} + \boldsymbol{v}\cdot\boldsymbol{p}_{loc}), \quad T_{couple} = \boldsymbol{\Omega}\cdot\pi_{shape} + \boldsymbol{v}\cdot\boldsymbol{p}_{shape}, \\ T_{shape} = \frac{1}{2}\oint_{\partial\mathscr{B}} \varphi_{shape}\frac{\partial \varphi_{shape}}{\partial n}\, \mathrm{d}s. \end{gathered} \tag{4.3}$$

If the prescribed shape deformations are to be maintained, the kinetic energy T_{shape} represents an energy input by the deformable body into the fluid. The energy input by the shape deformations T_{shape} sets the surrounding fluid into motion and part of this energy gets utilized by the net locomotion, that is, it gets transformed to T_{loc} via the coupling term T_{couple} between shape and net locomotion. Note that T_{couple} may be positive or negative. One can argue on physical grounds that in general, starting from rest with zero vorticity, a non-negative energy gets *lost* into creating the vortex wake. That is, part of T_{shape} gets transferred to the last term in (4.1), namely, to the kinetic energy of the wake $(1/2)\int_{\mathscr{F}} \boldsymbol{\psi}\cdot\boldsymbol{\omega}\, \mathrm{d}a$, via the coupling term $(1/2)\int_{\partial\mathscr{B}} \boldsymbol{u}_w \times \boldsymbol{\psi}\, \mathrm{d}s$. This means that, from an energy perspective, swimming in potential flow is most efficient in the sense that the energy input by shape deformations is transferred into energy utilized by net locomotion without losing energy to the wake. Indeed, this argument is employed in Wu (1971*a*, *b*) where he investigated energy-optimal shape changes.

5. Equations of motion in potential flow

Assume that the shape deformations do not generate vorticity in the fluid such that, starting with zero vorticity, the flow remains irrotational for all time and both $\boldsymbol{F}_w$ and $\boldsymbol{M}_w$ are identically zero. This assumption is physically meaningful only when the actual flow does not separate at the tail. That is, when the velocity of the fluid at the trailing edge is tangent to the spatial trajectory described by the trailing edge.

In potential flow, the balance laws (3.7) can be rewritten as

$$\frac{\mathrm{d}\boldsymbol{p}}{\mathrm{d}t} = 0, \quad \frac{\mathrm{d}\pi}{\mathrm{d}t} = 0, \tag{5.1}$$

where $\boldsymbol{p} = \boldsymbol{p}_{loc} + \boldsymbol{p}_{shape}$ and $\pi = \pi_{loc} + \pi_{shape}$. Equations (5.1) are equivalent to the balance laws derived in Kanso *et al.* (2005) for a system of articulated rigid links. To show this, it is convenient to use the body-fixed coordinates $\boldsymbol{X}$ measured from the body-fixed frame $\boldsymbol{b}_i$ whose origin is placed at $\boldsymbol{x}_o$. The potential function can be rewritten in body coordinates as follows:

$$\phi = \Omega\varphi_\Omega + V_1\varphi_1 + V_2\varphi_2 + \varphi_{shape}, \tag{5.2}$$

where

$$\frac{\partial \varphi_\Omega}{\partial n} = \boldsymbol{X}\times\boldsymbol{n}\cdot\boldsymbol{b}_3, \quad \frac{\partial \varphi_1}{\partial n} = \boldsymbol{n}\cdot\boldsymbol{b}_1, \quad \frac{\partial \varphi_2}{\partial n} = \boldsymbol{n}\cdot\boldsymbol{b}_2 \quad \text{on } \partial\mathscr{B}. \tag{5.3}$$

Express the shape momenta (3.10) in body frame where the components of the normal vector are given by (5.3),

$$\begin{aligned}\boldsymbol{\Pi}_{shape} &= \left(\oint_{\partial\mathscr{B}} \varphi_{shape}\frac{\partial\varphi_{\Omega}}{\partial n}\,\mathrm{d}s\right)\boldsymbol{b}_3,\\ \boldsymbol{P}_{shape} &= \left(\oint_{\partial\mathscr{B}} \varphi_{shape}\frac{\partial\varphi_{1}}{\partial n}\,\mathrm{d}s\right)\boldsymbol{b}_1 + \left(\oint_{\partial\mathscr{B}} \varphi_{shape}\frac{\partial\varphi_{2}}{\partial n}\,\mathrm{d}s\right)\boldsymbol{b}_2.\end{aligned} \tag{5.4}$$

Similarly, express the locomotion momenta (3.9) in body frame which, upon using (5.2) and (5.3), gives

$$\begin{pmatrix}\boldsymbol{\Pi}_{loc}\\ \boldsymbol{P}_{loc}\end{pmatrix} = \mathbb{I}_{loc}\begin{pmatrix}\boldsymbol{\Omega}\\ \boldsymbol{V}\end{pmatrix}, \quad \mathbb{I}_{loc} = \left(\begin{array}{c|cc} \oint \varphi_{\Omega}\frac{\partial\varphi_{\Omega}}{\partial n}\,\mathrm{d}s & \oint \varphi_{\Omega}\frac{\partial\varphi_{1}}{\partial n}\,\mathrm{d}s & \oint \varphi_{\Omega}\frac{\partial\varphi_{2}}{\partial n}\,\mathrm{d}s\\ \hline \oint \varphi_{1}\frac{\partial\varphi_{\Omega}}{\partial n}\,\mathrm{d}s & \oint \varphi_{1}\frac{\partial\varphi_{1}}{\partial n}\,\mathrm{d}s & \oint \varphi_{1}\frac{\partial\varphi_{2}}{\partial n}\,\mathrm{d}s\\ \oint \varphi_{2}\frac{\partial\varphi_{\Omega}}{\partial n}\,\mathrm{d}s & \oint \varphi_{2}\frac{\partial\varphi_{1}}{\partial n}\,\mathrm{d}s & \oint \varphi_{2}\frac{\partial\varphi_{2}}{\partial n}\,\mathrm{d}s \end{array}\right). \tag{5.5}$$

Note that the two components of the vectors $\boldsymbol{P}_{loc}$ and $\boldsymbol{V}$ occupy the second and third entries of $(\boldsymbol{\Pi}_{loc} \quad \boldsymbol{P}_{loc})^{\mathrm{T}}$ and $(\boldsymbol{\Omega} \quad \boldsymbol{V})^{\mathrm{T}}$, respectively. Also, note that $\mathbb{I}_{loc}$ is a 3×3 symmetric matrix referred to as the locked inertia matrix. One can readily verify, by definition and using the rigid transformation (2.8), that $\boldsymbol{P} = \boldsymbol{P}_{loc} + \boldsymbol{P}_{shape}$ and $\boldsymbol{\Pi} = \boldsymbol{\Pi}_{loc} + \boldsymbol{\Pi}_{shape}$ are related to $\boldsymbol{p}$ and π as follows:

$$\boldsymbol{p} = \boldsymbol{R}\boldsymbol{P}, \quad \pi = \boldsymbol{\Pi} + \boldsymbol{x}_o \times \boldsymbol{p}. \tag{5.6}$$

Substitute (5.6) into (5.1) to get that the later can be expressed in body frame in the form

$$\dot{\boldsymbol{P}} = \boldsymbol{P}\times\boldsymbol{\Omega}, \quad \dot{\boldsymbol{\Pi}} = \boldsymbol{P}\times\boldsymbol{V}. \tag{5.7}$$

These equations have the same form as Kirchhoff equations for the motion of a rigid body in potential flow and were derived in Kanso *et al.* (2005) using Hamilton's variational principle and a Lagrangian function equal to the kinetic energy (4.2) of the solid–fluid system (see also Miloh & Galper 1993; Galper & Miloh 1994 and references therein for applications of these equations to bubble dynamics and swimming problems). When the motion starts from rest, $\boldsymbol{P}$ and $\boldsymbol{\Pi}$ remain identically zero throughout the motion, hence the *reconstruction* equation

$$\begin{pmatrix}\boldsymbol{\Omega}\\ \boldsymbol{V}\end{pmatrix} = -\,\mathbb{I}_{loc}^{-1}\begin{pmatrix}\boldsymbol{\Pi}_{shape}\\ \boldsymbol{P}_{shape}\end{pmatrix}. \tag{5.8}$$

It is worth noting that (5.7) and (5.8) governing the motion in potential flow can be thought of in terms of gauge-theoretic methods of geometric mechanics and optimal control, as in the 'falling cat' problem (see Montgomery 1990). Gauge-theoretic methods were pioneered by Shapere & Wilczek (1987) for swimming at low Reynolds numbers and have only been applied sparingly since (see, e.g. Kelly 1998; Radford 2003; Kanso *et al.* 2005).

6. Examples of swimming in potential flow

We investigate the motion of a deformable body undergoing cyclic shape changes in potential flow ($\boldsymbol{F}_w$ and $\boldsymbol{M}_w$ are neglected).

6.1. *Large amplitude shape deformations*

The body is assumed to have an elongated geometry in its stretched-out reference configuration as shown in figure 3(*a*). It is convenient to write the shape deformations

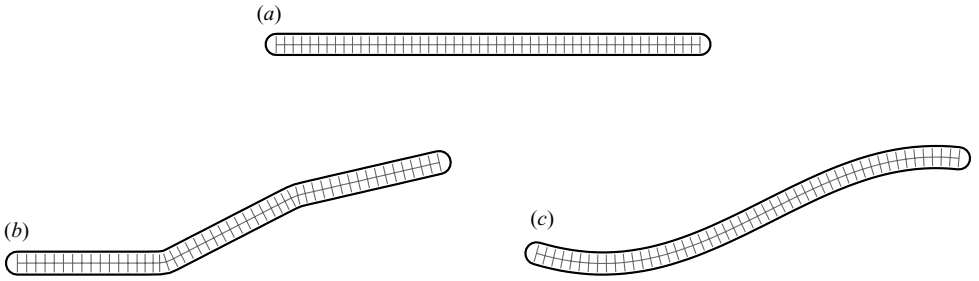

FIGURE 3. The body is assumed to have an elongated geometry in its stretched-out reference configuration as shown in (*a*). We investigate two types of large amplitude deformations of the centreline: flapping (*b*) and undulating (*c*). In (*a*), the centreline is first discretized into a number of line segments. The normal direction to each line segment of the centreline is computed as shown. The boundary points are specified along the normal directions at an offset distance a. The head and tail are semi-circles of radii equal a. To construct (*b*) and (*c*), a deformation is imposed on the discretized inextensible centreline. The boundary points are obtained using the orthogonality assumption: normal cross-sections to the centreline remain normal at all time. That is, the boundary points are specified along the (rotated) normal directions at an offset equal to a.

in body coordinate ((X_c, Y_c) of the centreline and (X_{shape}, Y_{shape}) of the boundary). The centreline is described by $X_c = s_c$, $Y_c = 0$ (the arclength s_c is given by $0 \leqslant s_c \leqslant l = 1$) and the boundary points are described by

$$X^{\pm}_{shape} = X_c, \quad Y^{\pm}_{shape} = \pm a, \tag{6.1}$$

where $\pm$ sign is used to denote the boundary points on both sides of the centreline and $2a$ is the body thickness. The head and tail are semi-circles of diameters equal to the thickness $2a$. The boundary of the body is a piecewise continuous curve whose perimeter and area in the reference configuration are $2l + 2\pi a$ and $al + \pi a^2$, respectively. This choice of geometry is made for simplicity but the numerical method proposed below can be used for any prescribed geometry of the deformable body – in particular, one could use geometry profiles of actual fish.

Within the class of swimming due to transverse deformations of fish body, biologists identify two types of swimming mechanisms: undulatory motions consisting of a travelling wave along the fish body and oscillatory or flapping motions of the fish tail (see Sfakiotakis, Lane & Davies 1999). Further, fish locomotion can be classified based on the swimming temporal features: periodic swimming characterized by cyclic repetitive movements or transient movements typically used in rapid starts, escape maneuvers or turns. In this section, we focus on studying periodic swimming by prescribing two types of cyclic shape changes $X_c(s_c, t)$ and $Y_c(s_c, t)$ of the centreline: flapping and undulating. Flapping motions consist of deformations induced by activating a finite number of joints along the centreline and are similar to those considered in Kanso *et al.* (2005) for a three-link body. In particular, we consider the shape deformations induced by two joints located at positions $s_c = l_1$ and $s_c = l_2$. These joints allow relative rotations of the body described by

$$\theta_1 = \Theta_1 \cos(2\pi t), \quad \theta_2 = \Theta_2 \cos(2\pi t - \alpha), \tag{6.2}$$

where θ_1 and θ_2 are the relative angles at the joints as depicted in figure 3(*b*), Θ_1 and Θ_2 denote the amplitude of flapping and α denotes the phase. Recall that t represents dimensionless time dictated by $t = f\tau$ where f is a flapping frequency (in Hz) and τ is real time.

Undulatory motions consist of travelling waves of the centreline similar to those considered in Wu (1971*a*) but, unlike Wu's small amplitude deformations for which $X_c = s_c$ is constant, here both $X_c(s_c, t)$ and $Y_c(s_c, t)$ vary with time (see figure 3*c*). In particular, we consider deformations of the centreline of the form

$$Y_c = A\cos(2\pi t - \kappa X_c), \tag{6.3}$$

which represents a wave propagating along the planar body with phase velocity $2\pi/\kappa$.

The deformations $X_c(s_c, t)$ and $Y_c(s_c, t)$ of the centreline for the flapping and undulatory motions are completely determined by using (6.2) and (6.3), respectively, and imposing the inextensibility condition. The corresponding boundary points $X_{shape}(s, t)$ and $Y_{shape}(s, t)$ are obtained numerically using the orthogonality assumption where cross-sections normal to the centreline remain normal at all time (see figure 3). More specifically, the centreline is first discretized into a number of line segments. The normal direction to each segment is computed at each time step. The boundary points are specified along the normal directions at an offset equal to the thickness a of the body.

6.2. *Numerical method*

In potential flow, the fluid velocity $\boldsymbol{u} = \nabla\phi$ is given by the potential function ϕ, which can be constructed using (5.2) from the velocity potentials φ_1, φ_2, φ_Ω and φ_{shape}. The problem of solving Laplace's equation for the velocity potentials over the fluid domain $\mathscr{F}$ subject to zero velocity at infinity and boundary conditions (5.3) and $\nabla\varphi_{shape}\cdot\boldsymbol{n}|_{\partial\mathscr{B}} = \boldsymbol{V}_{shape}\cdot\boldsymbol{n}$ can be solved numerically using a *boundary element method*, also referred to as a panel method. We use the panel method devised by Hess & Smith (1966) (see also Katz & Plotkin 2001) which utilizes a piecewise-constant distribution of *source singularities* over the boundary of the submerged body and computes the strength of this distribution by imposing appropriate boundary conditions. The use of source/sink distributions cannot contribute any net circulation around the body and allows one to ensure *a priori* that the circulation in the fluid remains zero at all time. Physically speaking, this *fictitious source distribution* induces a velocity field in the fluid that is equivalent to the velocity field resulting from the motion of the submerged body. The theoretical foundation of such panel methods is based on reformulating Laplace's equations as a boundary integral equation, using the divergence theorem (see, e.g. Moran 1984, chapter 6). As a result, only the boundary of the submerged body need to be discretized, hence the computational advantages of such method. Some of the other advantages of this numerical method lies in the freedom it provides for describing the geometry of the deformable body and that it can readily accommodate for the presence of vorticity (with bounded support) when included in the model as done in § 7.

Traditionally, these panel methods are used for rigid bodies where the panels maintain a fixed length throughout the calculation. The body deformations considered here may cause the boundary perimeter to vary with time (while enclosing a region of constant area and maintaining an inextensible centreline). In our calculations, we fix the total number of panels used to discretize the boundary but allow their length to change with time (220 panels are used, each of length 0.01 approximately). The variation of the panel length in time has no effect on the dynamics because the potential flow only depends on the instantaneous geometry of the deformable body. We carried several numerical tests on standard examples of an ellipse with variable major and minor axes to validate our code. When point vortices are included in the fluid domain as done in § 7, we tested our code using the example of a circle

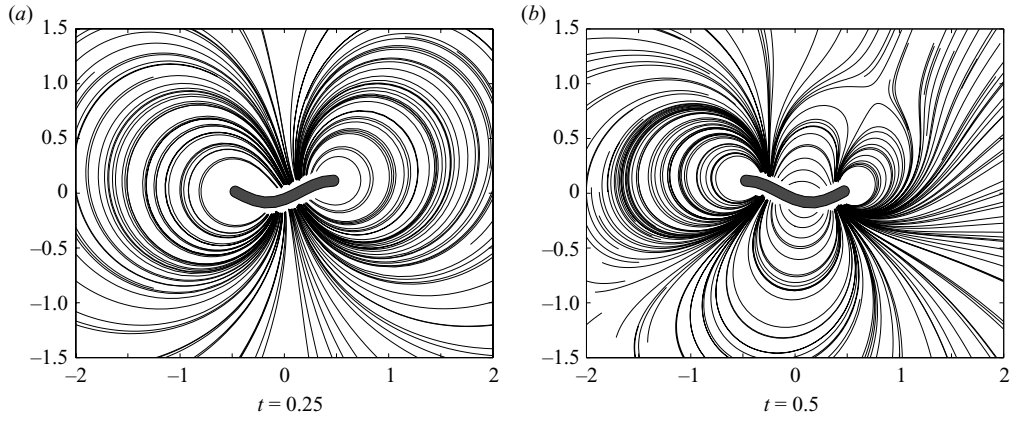

FIGURE 4. Snapshots of the streamlines at $t = 0.25$ and $t = 0.5$ corresponding to fluid motion induced by undulating shape deformations of the form $Y_c = 0.1\cos(2\pi(t - 0.8\boldsymbol{x}_c))$.

interacting with point vortices which admits an analytical solution based on the Milne–Thompson circle theorem.

For the deformable body examples discussed in § 6.3, we solve for four distinct source distributions corresponding the four velocity potentials φ_1, φ_2, φ_Ω and φ_{shape} subject to four sets of boundary conditions: zero velocity at infinity and boundary conditions (5.3) for $\varphi_\Omega, \varphi_1, \varphi_2$, respectively, and $\nabla\varphi_{shape} \cdot \boldsymbol{n}|_{\partial\mathcal{B}} = \boldsymbol{V}_{shape} \cdot \boldsymbol{n}$ for φ_{shape}. Figure 4 depicts snapshots of the streamlines corresponding to fluid motion (φ_{shape} only) induced by undulating shape deformations of the form $Y_c = 0.1\cos(2\pi(t - 0.8X_c))$. The body length (that is, the length of the centreline) is normalized to $l = 1$ and the thickness is set to $2a = 0.1$.

6.3. *Numerical results and discussion*

We compute the net locomotion (β, x_o, y_o) of the deformable body due to prescribed shape deformations of two types: flapping and undulating. The deformable body is assumed to start from rest (zero momentum). The velocity potentials are solved at each time step using the panel method described above. The shape momenta of (5.4) and the added mass $\mathbb{I}_{loc}$ of (5.5) are then computed and used to obtain the body velocities in (5.8). A standard fourth-order Runge–Kutta integration scheme with constant time step is used to integrate (5.8) and obtain (β, x_o, y_o). For all trajectories shown in this section, the total integration time is $t = 10$. The value of a is set to 0.01, the length l of the centreline is normalized to $l = 1$.

The net locomotion of the deformable body in the $(\boldsymbol{e}_1, \boldsymbol{e}_2)$ plane due to prescribed flapping motion is shown in figure 5. The parameters of the shape deformations are set to $\Theta_1 = \Theta_2 = 0.5$ and $\alpha = \pi/4$, that is, $\theta_1 = 0.5\cos(2\pi t)$ and $\theta_2 = 0.5\cos(2\pi t - \pi/4)$. The trajectories in figure 5 are obtained by varying the position of the joints along the centreline. Recall that the joints are placed at $s_c = l_1$ and $s_c = l_2$, which can also be parameterized by $l_{head} = l_1$, $l_{middle} = l_2 - l_1$ and $l_{tail} = l - l_2$, that is, the length of the front, middle and rear portions of the body, respectively (only two parameters are needed since the total length l is fixed). The nine depicted cases correspond to

$$\begin{cases} l_{head} = 1/3,\ 1/2,\ 2/3, \\ l_{tail} = (l - l_{head})/3,\ (l - l_{head})/2,\ 2(l - l_{head})/3 \end{cases}.$$

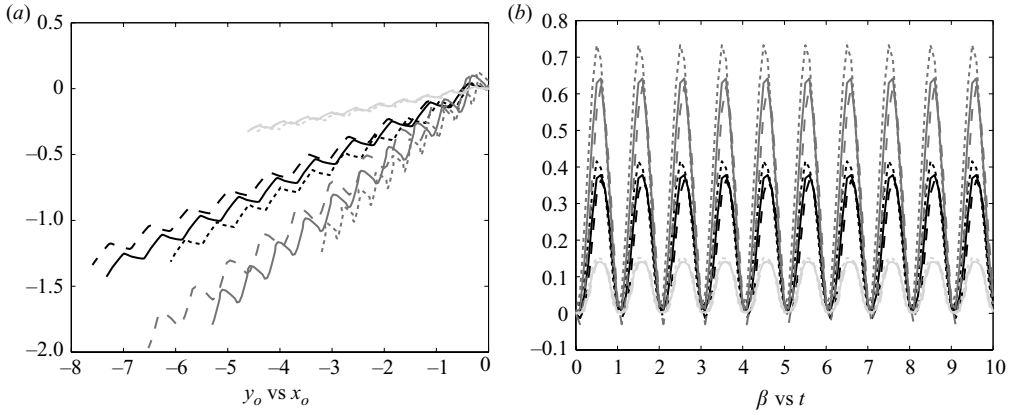

FIGURE 5. Flapping motions. (*a*) Net locomotion of the deformable body in the $(\boldsymbol{e}_1, \boldsymbol{e}_2)$. (*b*) Rotation β versus time t. The values of a and l are set to $a = 0.01$ and $l = 1$. The shape deformations are $\theta_1 = 0.5\cos(2\pi t)$, $\theta_2 = 0.5\cos(2\pi t - \pi/4)$. Nine distinct trajectories are shown corresponding to: (black lines) $l_{head} = 1/2$, (medium grey lines) $l_{head} = 1/3$ and (light grey lines) $l_{head} = 2/3$ while (solid lines) $l_{tail} = (l - l_{head})/2$, (wide dashed lines) $l_{tail} = 2(l - l_{head})/3$ and (narrow dashed lines) $l_{tail} = (l - l_{head})/3$.

We define the travelled distance as the shortest distance from the initial position at (0, 0) to the final position along a given trajectory. One observes the following:

(i) For l_{head} fixed, the travelled distance is maximum for the longest tail.

(ii) For l_{tail} fixed, the travelled distance is maximum for $l_{head} = 1/2$.

(iii) The amplitude of β increases as l_{head} decreases.

These results are consistent with observations of actual fish that use such flapping motions for swimming (that is, Carangiform and Thunniform swimmers). These fish typically use the last third of their body length to flap (of which the tail occupies the larger portion) while most of their body mass is concentrated in the anterior part in order to minimize the sideways oscillations β (see, e.g. Sfakiotakis *et al.* 1999).

The effect of the phase α on the net locomotion is now examined. As before, the amplitude of the shape deformations is set to $\Theta_1 = \Theta_2 = 0.5$. The prescribed shape angles $\theta_1 = 0.5\cos(2\pi t)$ and $\theta_2 = 0.5\cos(2\pi t - \alpha)$ trace elliptic closed curves in the (θ_1, θ_2) plane. These closed curves are traced in the counter-clockwise direction. The curves corresponding to $\alpha = 0$ and $\alpha = \pi$ are bounded line intervals along $\theta_2 = \theta_1$ and $\theta_2 = -\theta_1$, respectively. For $\alpha = \pi/2$, θ_1 and θ_2 trace a circle in the (θ_1, θ_2) plane. For all other α, θ_1 and θ_2 trace ellipses which are symmetric with respect to reflections across the axes $\theta_2 = \theta_1$ and $\theta_2 = -\theta_1$. That is, the shape curves are ellipses whose major axes form angles $\pi/4$ or $3\pi/4$ with the θ_1-axis. Their semi-axes lengths are dictated by the value of α. The phase angle α is varied from 0 to π by increments of $\Delta\alpha = \pi/24$. Three different joint positions are examined corresponding to

$$\begin{cases} l_{head} = 1/3,\ l_{tail} = 1/3 \\ l_{head} = 1/2,\ l_{tail} = 1/4 \\ l_{head} = 2/3,\ l_{tail} = 1/6 \end{cases}.$$

A plot of the travelled distance versus α is shown in figure 6(*a*) for the three parameter sets. Figure 6(*b*) shows the mean values of the energy input T_{shape} due to shape deformations (solid lines) and the energy associated with the net locomotion T_{loc} (dashed lines). Figure 6(*b*) reinforces the argument presented in § 4 that, in potential flow, most of the energy input by the shape deformations is transformed into energy

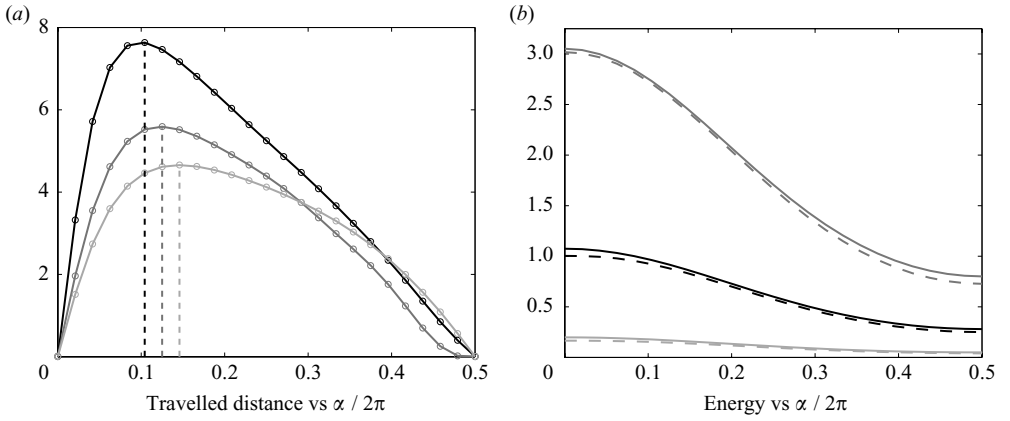

FIGURE 6. Flapping motion. (a) travelled distance versus phase angle α. (b) Mean values of the energy input T_s (solid lines) and energy associated with the net locomotion T_{loc} (dashed lines) versus phase angle α. Three distinct cases are analysed corresponding to: (black lines) $l_{head} = 1/2$, $l_{tail} = 1/4$, (medium grey lines) $l_{head} = 1/3$, $l_{tail} = 1/3$ and (light grey lines) $l_{head} = 2/3$, $l_{tail} = 1/6$.

used by the body locomotion. It is worth clarifying here that the term locomotion is used to signify a rigid motion (displacement and rotation) of the body. However, not every shape deformation results in a useful rigid motion – for example, it is clear from figure 6(a) that, for $\alpha = 0$ and $\alpha = \pi$, the distance travelled over 10 cycles (or periods) of shape deformations is zero while figure 6(b) shows that the mean value of T_{loc} is not zero. For these special cases, the body undergoes a rigid motion (hence the non-zero T_{loc}) but such that it returns to its initial position and orientation after a complete cycle of shape deformations (hence the zero travelled distance or zero *net* locomotion). This is due to the reversibility of motion in potential flow when reversing the boundary conditions, that is, time reversibility of the employed model. This reversibility property in potential flow is analogous to the reversibility in Stokes' flow described in Purcell (1977). Purcell states that *if a body changes its shape then goes back to its original shape by going through the sequence of shape motion in reverse, everything reverses just fine. Time makes no difference – only configuration.* This is also true in potential flow. The speed at which the shape deformations take place is not important, only the pattern of shape motion matters. The travelled distance is invariant to time re-parameterization. It also follows from this time reversibility that the deformable body moves to the left in the $(\boldsymbol{e}_1, \boldsymbol{e}_2)$ plane for $0 \leqslant \alpha \leqslant \pi$ while it moves to the right symmetrically about the origin when the phase is set to $-\alpha$. For this reason, we only show the results corresponding to $0 \leqslant \alpha \leqslant \pi$.

The value of α corresponding to the maximum travelled distance is highlighted in figure 6(a) for each of the three depicted cases. The body for which $l_{head} = 1/2, l_{tail} = 1/4$ travels longer distance than the other two bodies for almost all α and reaches its maximum travelled distance at $\alpha_c = 5\pi/24$. The body for which $l_{head} = 1/3, l_{tail} = 1/3$ (that is, body with three equal segments) reaches its maximum travelled distance at $\alpha_c = \pi/4$ and the third body at $\alpha_c = 7\pi/24$. One could think of the values of α_c as the *optimal* phase values for the corresponding body geometries and class of shape deformations, namely, $\theta_1 = \Theta_1 \cos(2\pi \boldsymbol{t})$ and $\theta_2 = \Theta_1 \cos(2\pi t - \alpha)$. In figure 7, we plot the shape cycles corresponding to α_c. These optimal cycles are ellipses whose major axes form an angle $\pi/4$ with the θ_1-axis. This is consistent with

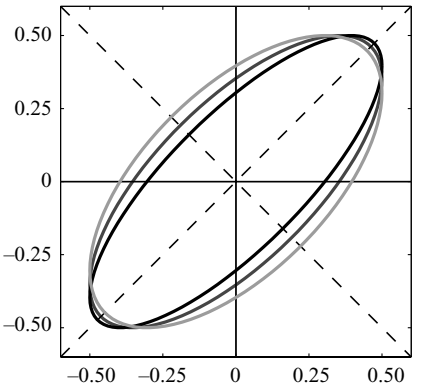

FIGURE 7. Flapping motion. Optimal shape cycles in the (θ_1, θ_2) plane corresponding to the maximum travelled distance in figure 6(a): (black line) $l_{head} = 1/2$, $l_{tail} = 1/4$ and $\alpha_c = 5\pi/24$; (medium grey line) $l_{head} = 1/3$, $l_{tail} = 1/3$ and $\alpha_c = \pi/4$; and (light grey line) $l_{head} = 2/3$, $l_{tail} = 1/6$ and $\alpha_c = 7\pi/24$. The deformable body moves to the left in the $(\boldsymbol{e}_1, \boldsymbol{e}_2)$ plane when the depicted shape trajectories are traced in the counter-clockwise direction and to the right otherwise.

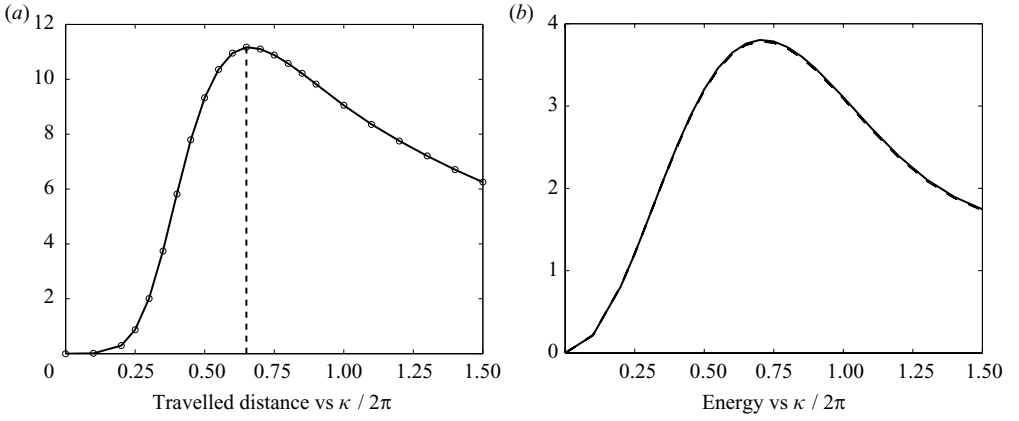

FIGURE 8. Undulatory motion. (a) Travelled distance versus wavelength κ. (b) Mean values of the energy input T_{shape} (solid lines) and energy associated with the net locomotion T_{loc} (dashed lines) versus wavelength κ.

the findings in Tam & Hosoi (2007) where the optimal shape patterns for Purcell's three-link swimmer in Stokes' flow are ellipse-like curves with major axes of symmetry at an angle $\pi/4$ with the θ_1-axis. The question whether this is a preferred direction across the whole range of Reynolds number from Stokes' to Potential flow remains open.

The trajectories for the net locomotion (not shown) of the deformable body in the $(\boldsymbol{e}_1, \boldsymbol{e}_2)$ plane due to prescribed undulatory motions are similar to those obtained in figure 5 for flapping motions. A plot of the travelled distance versus the wavelength κ is shown in figure 8(a) where κ is varied from 0 to 1.5 and A is set to 0.1. The undulating body achieves a maximum travelled distance when $\kappa = 0.65(2\pi) = 1.3\pi$. In figure 8($b$) there is a depiction of the mean values of the energy input T_{shape} due to shape deformations (solid lines) and the energy associated with the net locomotion T_{loc} (dashed lines) versus the wavelength κ. Similarly to figure 6(b), most of the energy

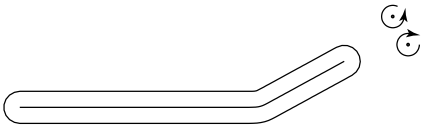

FIGURE 9. A vortex pair is shed periodically when the tail reaches its maximum and minimum flapping angle.

input by T_{shape} is transformed into energy used by T_{loc}. One should be careful not to compare the case when $\alpha = 0$ in figure 6 to that when $\kappa = 0$ in figure 8. For $\alpha = 0$ (and π), the body is flapping and the energy input is non-zero but for $\kappa = 0$, there is no shape deformations ($y_c = 0$) and no locomotion. The case where the body behaves as a rigid rod flapping against the fluid does not correspond to $\kappa = 0$ and is not represented in figure 8. This case results in zero net locomotion (but non-zero energy) owing to the reversibility property discussed above. To conclude this discussion, note that there is a common belief that the flapping motions evolved from the undulatory ones as a more efficient mechanism for locomotion (see Sfakiotakis *et al.* 1999). The optimal trajectories in figures 6 and 8 show that, indeed, the flapping case with $l_{head} = 2/3$ (consistent with Carangiform and Thunniform swimmers) requires the least energy per distance travelled. Note that one could think of the undulatory motion as a special case of the flapping motion in the limit when the number of joints (or links) goes to infinity. A more rigorous comparison of the efficiency of locomotion between the flapping and undulating case could then be sought.

7. Swimming due to dipole shedding

We propose a simple model to emulate the locomotion of a deformable body under the effect of its own vortex wake. The proposed model is not intended to study the details of vortex shedding (which is a complicated event involving flow separation at the tail) but focuses on the effects of the shed vortices on the net locomotion. The model consists of a body (say having the same geometry as in § 6) allowed to undergo shape deformations such that a new vortex pair (a dipole) is 'shed' from the tail (i.e. introduced into the flow) each time the tail reaches its minimum and maximum flapping angle (see figure 9) while old vortex pairs are removed from the flow as they move away from the body. The introduction of vortex pairs emulates the vortices shed periodically due to the flapping motion of the body. The removal of vorticity emulates the diminishing effect of the vortices far away from the body. The dipole model is chosen for two reasons: (i) there is experimental evidence that fish and flapping airfoils shed a dipole every half cycle of their oscillation (see, e.g. Tytell 2004; Tytell & Lauder 2004) and (ii) it guarantees that no circulation is introduced into the fluid domain, thus satisfying Kelvin's circulation theorem.

Between two consecutive shedding events, the system corresponds to a deformable body dynamically interacting with $2N$ point vortices of strength Γ_k ($k = 1, \ldots, 2N$) such that the sum of their strength is zero. Let the position vectors of the point vortices be denoted by $\boldsymbol{x}_k$ in the inertial frame $\{\boldsymbol{e}_i\}$ and $\boldsymbol{X}_k$ in the body-fixed frame $\{\boldsymbol{b}_i\}$. The vorticity $\boldsymbol{\omega}$ is given by a delta distribution $\boldsymbol{\omega} = \sum_{k=1}^{2N} \Gamma_k \delta(\boldsymbol{x} - \boldsymbol{x}_k)\boldsymbol{e}_3$. Substitute this expression for the vorticity into (3.7) to get that the latter can be rewritten in the same convenient form as shown in (5.1) but with the total momenta of the body–fluid

system given by

$$\begin{aligned} \boldsymbol{p} &= \boldsymbol{p}_{loc} + \boldsymbol{p}_{shape} + \frac{\mathrm{d}}{\mathrm{d}t}\oint_{\partial\mathscr{B}} \boldsymbol{x}\times(\boldsymbol{n}\times\boldsymbol{u}_w)\,\mathrm{d}s + \sum \Gamma_k \boldsymbol{x}_k \times \boldsymbol{e}_3, \\ \pi &= \pi_{loc} + \pi_{shape} - \frac{1}{2}\oint_{\partial\mathscr{B}} \|\boldsymbol{x}\|^2(\boldsymbol{n}\times\boldsymbol{u}_w)\,\mathrm{d}s - \frac{1}{2}\sum \Gamma_k(\boldsymbol{x}_k\cdot\boldsymbol{x}_k)\boldsymbol{e}_3. \end{aligned} \tag{7.1}$$

The linear and angular momenta of the body–fluid system are assumed to remain constant during vortex shedding, which takes place instantaneously when the tail reaches its maximum flapping amplitude. That is, at the time of the shedding $t_{shedding}$ the body–fluid momenta immediately after the vortex shedding are equal to those immediately before the shedding,

$$\boldsymbol{p}|_{t^+_{shedding}} = \boldsymbol{p}|_{t^-_{shedding}}, \qquad \pi|_{t^+_{shedding}} = \pi|_{t^-_{shedding}}. \tag{7.2}$$

Equations (7.2) are used to determine the jump in the translational and rotational velocity of the body at each shedding event. Note that this model for vortex shedding is analogous to the perfectly elastic impact model between colliding bodies where the impact is assumed to take place instantaneously and the total momentum of the colliding bodies is assumed to be constant during the impact. Theoretically, one could introduce, similar to the *coefficient of restitution* concept in colliding bodies, a parameter that accounts for the change in the momentum of the solid–fluid system during a shedding event.

In order to close the model, one needs to provide the equations governing the motion of the vortices between two consecutive shedding events. This closure is given by the fact that point vortices are advected by the flow, hence,

$$\frac{\mathrm{d}\boldsymbol{x}_k}{\mathrm{d}t} = \boldsymbol{u}|_{\boldsymbol{x}_k}, \tag{7.3}$$

where the velocity $\boldsymbol{u}$ at the point vortex $\boldsymbol{x}_k$ is due to the motion of the body (both shape deformation and net locomotion) and the presence of the other point vortices (excluding the effect of a point vortex on itself).

It is worth noting that, when transformed to body frame, (5.1), (7.1) and (7.3) are consistent with the balance laws derived in Shashikanth *et al.* (2002) and Kanso & Oskouei (2008) for a rigid body interacting with point vortices. In the rigid-body case, $\boldsymbol{p}_{shape}$ and π_{shape} as well as $\boldsymbol{P}_{shape}$ and $\boldsymbol{\Pi}_{shape}$ are identically zero.

In order to isolate the effect of the vortex shedding on the net locomotion, we consider a class of shape deformations that cannot produce a net displacement in the absence of vortex shedding. In particular, only the tail of the body is allowed to flap such that

$$\theta = \Theta\cos(2\pi t), \tag{7.4}$$

in contrast to (6.2) where two shape angles θ_1 and θ_2 are varied with time. The deformable body is assumed to start from rest (zero momentum). The velocity potentials subject to zero velocity at infinity and proper boundary conditions at the body's boundary are computed at each time step using the panel method described in § 6. The main difference in the numerical method is that, here, one has to account for the presence of the vortex singularities in the flow when computing the strength of the *source singularity* distribution over the boundary of the submerged body. The shape momenta of (5.4) and the added mass $\mathbb{I}_{loc}$ of (5.5) are then computed. Also, the tangential component of the velocity $\boldsymbol{u}_w$ is computed and used to evaluate the integral quantity in (7.1). At $t_{shedding}$, (7.2) is used to compute the jump in the body's linear and

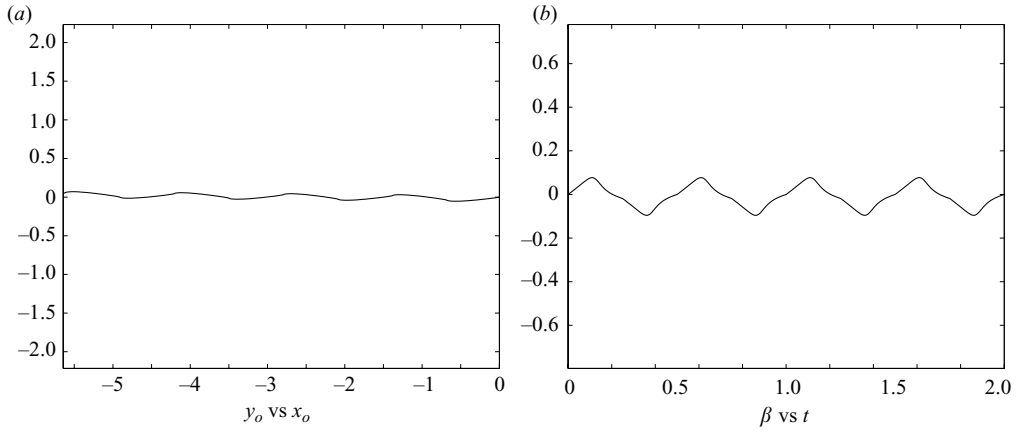

FIGURE 10. Locomotion due to the effect of dipole shedding: (*a*) the motion of the body in the $(\boldsymbol{e}_1, \boldsymbol{e}_2)$ plane; (*b*) the variation of β with respect to time.

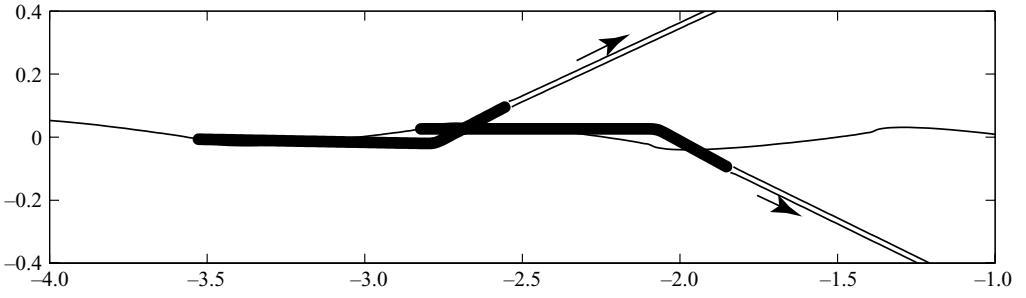

FIGURE 11. Zoom in on figure 10(*a*): a dipole is shed periodically when the tail reaches its maximum and minimum flapping angle as depicted here for two consecutive shedding events. The shed dipole moves away from the body as the body moves to the left.

angular velocity. Between two consecutive shedding events, a standard fourth-order Runge–Kutta integration scheme with constant time step is used to integrate (5.1) (with $\boldsymbol{p}$ and π given by (7.1)) and (7.3) and to obtain (β, x_o, y_o) and $\boldsymbol{x}_k \equiv (x_k, y_k)$.

In figure 10–12, the total integration time is $t = 2$. As before, the length l of the centreline is normalized to $l = 1$ and the value of a is set to 0.01. The flapping amplitude is chosen to be $\Theta = 0.5$ rad. The dipole strength is set to $\Gamma = \pm 1$. At the time that a new dipole is shed, the old dipole is removed from the fluid instantaneously such that, at any instant in time, the body is interacting with only one vortex pair ($N = 1$). Figure 10 depicts the net motion of the body in the $(\boldsymbol{e}_1, \boldsymbol{e}_2)$ plane under the effect of vortex shedding. In figure 11, we zoom in on a portion of the trajectory shown in figure 10(*a*) on which we superimpose the body's configuration at two consecutive shedding events and show the trajectories traced by the shed dipoles. Clearly, the shed dipoles move away from the body as the body swims to the left. We tested various parameter values for Γ (not shown) and obtained similar behaviour to that shown in figures 10–12 for a range of values. Outside this range, the vortices are either too weak to move away from the body or too strong to allow the body to swim away (the body gets absorbed by the vortices). Fish also seem to be able to manipulate the intensity of the shed vortices within limits dictated by their muscles strength. Figure 12 depicts the linear and angular velocities of the body as they vary with time.

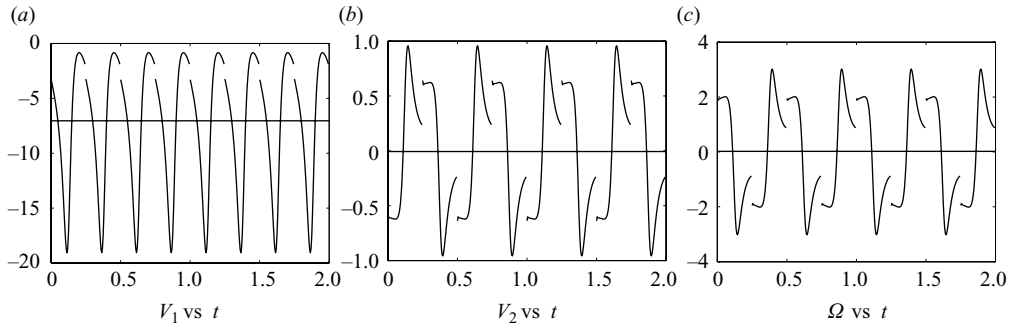

FIGURE 12. Linear and angular velocities with respect to time. Note the jump in the velocities at each shedding event. The average velocity V_1 is negative while the average of V_2 is almost zero, causing the body to undergo a net displacement in the negative $\boldsymbol{e}_1$-direction as shown in figure 10(a). Also, the average of Ω is zero which means that, while the body oscillates as it flaps, it undergoes no net reorientation as shown in figure 10(b).

Note the jump in the velocities at each shedding event. Also note the periodicity of these velocities as a function of time. This periodicity seems to suggest that the net locomotion may be described as a gauge over cyclic variations in shape. In general, the gauge-theoretic methods of geometric mechanics used to analyse motion in potential flow (Kelly 1998; Radford 2003; Kanso *et al.* 2005) may not be always applicable in the presence of vorticity. Indeed, if the fish flaps once or twice then stops flapping, it continues to interact dynamically with the vortices present in the fluid but these vortices drift away from the body of the fish which, in the mathematical modelling, gives rise to what is known as *dynamical systems with drift*. However, in the case of sustained swimming considered here, the fish is continuously shedding vortices with every half cycle of its shape deformation. One may then argue that the wake is also changing cyclically and hence, one may apply gauge-theoretic methods to analyse the net locomotion. These methods are particularly useful in studying the dependence of the system on parameters such as the amplitude/frequency of shape oscillations and strength/relative positions of dipoles and addressing problems of control and motion planning. These issues will be addressed in a future work.

8. Summary

Balance laws are derived for the swimming of a deformable body due to prescribed shape deformations and the wake vorticity. The derived equations can be viewed as a generalization of Lighthill's slender body theory and, in the potential flow case, reduce to the model developed in Kanso *et al.* (2005). The effect of cyclic shape changes on the locomotion of a deformable body in potential flow is examined via a number of examples. In particular, we compute optimal parameter values within a class of flapping motions and a class of undulatory motions. A direct comparison of the energy input per total distance travelled supports a common belief that flapping motions constitute a more efficient mechanism for locomotion than undulatory motions. The effect of a vortical wake on the net locomotion is modelled using a simplified approach where pairs of point vortices are shed periodically from the tail of the deformable body. In sustained/periodic swimming, fish continuously shed vortices of opposite strength that typically pair up to move away from the swimming fish whereas far downstream (i.e. the far-wake), viscous effects effectively

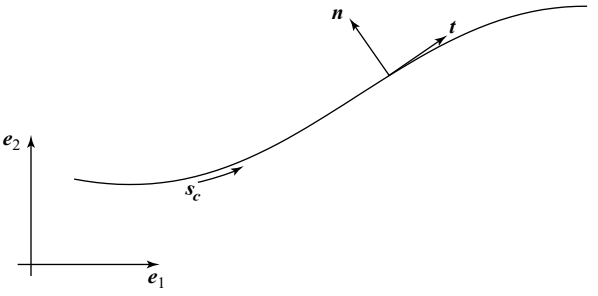

FIGURE 13. Lighthill's slender body.

diminish the presence of the vortices. The swimming motion is thus most affected by the most recently shed vortices. Our models capture exactly this aspect and show that both the shed vortices and the reaction forces (proportional to the added mass effect) play a role in swimming due to transverse shape deformations. Future extensions of this work will include more accurate models of vortex shedding and of decay of vortices due to viscous effects. We are also working on generalizing these methods to study the coupled dynamics of multiple submerged bodies and their wakes in an effort to model fish schooling.

I would like to thank Professors J. E. Marsden and B. N. Shashikanth for their useful comments and suggestions on an earlier version of this paper. I am also indebted to Professor P. K. Newton for many useful discussions. This work is partially supported by NSF through the award CMMI 06-44925.

Appendix. Lighthill's slender body theory

Lighthill's reactive force theory for the swimming of a slender body can be viewed as a special case of (3.7). To show this, first consider the setting employed in Lighthill (1975, chapter 5) of a 'spinal cord' of length l (which corresponds to the centreline of figure 1) undergoing large amplitude deformations (see figure 13). The normal and tangential components of the velocity $\boldsymbol{v}_{shape}$ of the centreline due to shape deformations are given by

$$\begin{aligned} v_{sn} &= \boldsymbol{v}_{shape} \cdot \boldsymbol{n} = \frac{\partial y_c}{\partial t}\frac{\partial x_c}{\partial s_c} - \frac{\partial x_c}{\partial t}\frac{\partial y_c}{\partial s_c}, \\ v_{st} &= \boldsymbol{v}_{shape} \cdot \boldsymbol{t} = \frac{\partial x_c}{\partial t}\frac{\partial x_c}{\partial s_c} + \frac{\partial y_c}{\partial t}\frac{\partial y_c}{\partial s_c}. \end{aligned} \tag{A 1}$$

Lighthill's theory lays principal emphasis on the reactive forces between the body and the volume of fluid in contact with it. These reactive forces are proportional to the added mass of fluid which acquires momentum through shape deformations. According to Lighthill, the essential property characteristic of an elongated body is that the added mass due to v_{sn}, that is, to deformations in the direction normal to the centreline, is large whereas the deformations tangential to the centreline have negligible added mass. The momentum $\boldsymbol{p}_{shape}$ of (3.10) can then be approximated by

$$\boldsymbol{p}_{shape} = \int_0^l m v_{sn} \boldsymbol{n} \, \mathrm{d}s_c \tag{A 2}$$

where m is the added mass per unit length of the centreline due to shape deformations only. In general, $m(s_c, t)$ is a function of arclength s_c and time t (m depends on φ_{shape}). In Lighthill (1975, chapter 4), the amplitude of the shape deformations is assumed to be steady in time and the approximate expression $m = (1/4)\pi\rho_f d^2$, where ρ_f is the fluid density (here normalized to one) and d is the depth of the cross-section, is used.

Lighthill avoided solving for the complex wake dynamics by considering the momentum balance in a control volume containing the deformable body and bounded by a plane attached at its trailing edge. This allows one to obtain an approximate expression for the rate of change of the momentum in the wake or $\boldsymbol{F}_w$

$$\boldsymbol{F}_w = \left[-m v_{sn} v_{st} \boldsymbol{n} - \frac{1}{2} m v_{sn}^2 \boldsymbol{t}\right]_{s_c = l}. \tag{A 3}$$

Substitute (A 2) and (A 3) in the balance of linear impulse of (3.7) to obtain the total forces acting on the slender body and causing it to achieve a net locomotion

$$\boldsymbol{F} = -\frac{\mathrm{d}}{\mathrm{d}\boldsymbol{t}} \int_0^l m v_{sn} \boldsymbol{n} \, \mathrm{d}s_c - \left[-m v_{sn} v_{st} \boldsymbol{n} - \frac{1}{2} m v_{sn}^2 \boldsymbol{t}\right]_{s_c = l} \tag{A 4}$$

Equation (A 4) is exactly the main balance law in Lighthill's slender body theory and can be viewed as a special case of the balance of linear impulse in (3.7). Equations (3.7) are more general in the sense that they account for the dynamic coupling of the rotational and translational motions whereas Lighthill's slender body theory focused only on the translational motion and neglected the rotational effects induced by the shape deformations on the net locomotion. Further, (3.7) hold in two-dimensional and three-dimensional while Lighthill's theory is specific to slender bodies as manifested by the approximate expressions for $\boldsymbol{p}_{shape}$ and $\boldsymbol{F}_w$. Our approach, instead of using such approximate analytical expressions, consists of employing (3.7) in conjunction with a numerical method that accurately computes $\boldsymbol{p}_{shape}$ and π_{shape} as well as $\boldsymbol{F}_w$ and $\boldsymbol{M}_w$.

REFERENCES

Borisov, A. V. & Mamaev, I. S. 2003 An integrability of the problem on motion of cylinder and vortex in the ideal fluid. *Regular Chaotic Dyn.* **8**, 163–166.

Eldredge, J. D. 2008 Dynamically coupled fluid–body interactions in vorticity-based numerical simulations. *J. Comput. Phys.* **227**, 9170–9194.

Galper, A. & Miloh, T. 1994 Generalized Kirchhoff equations for a deformable body in a weakly non-uniform flow field. *Proc. R. Soc. Lond.* A **446**, 169–193.

Hess, J. L. & Smith, A. M. O. 1966 Calculation of potential flow about arbitrary bodies. *Prog. Aeronaut. Sci.* **8**, 1–139.

Jones, M. A. 2003 The separated flow of an inviscid fluid around a moving flat plate. *J. Fluid Mech.* **496**, 405–441.

Kanso, E., Marsden, J. E., Rowley, C. W. & Melli-Huber, J. 2005 Locomotion of articulated bodies in a perfect fluid. *J. Nonlinear Sci.* **15**, 255–289.

Kanso, E. & Oskouei, B. 2008 Stability of a coupled body-vortex system. *J. Fluid Mech.* **600**, 77–94.

Katz, J. & Plotkin, A. 2001 *Low-Speed Aerodynamics*. Cambridge Aerospace Series.

Katz, J. & Weihs, D. 1978 Hydrodynamic propulsion by large amplitude oscillation of an airfoil with chordwise flexibility. *J. Fluid Mech.* **88** (3), 485–497.

Katz, J. & Weihs, D. 1979 Large amplitude unsteady motion of a flexible slender propulsor. *J. Fluid Mech.* **90** (4), 713–723.

Kelly, S. D. 1998 The mechanics and control of robotic locomotion with applications to aquatic vehicles. PhD thesis, California Institute of Technology.

Lamb, H. 1932 *Hydrodynamics*, 6th ed. Dover.

Lighthill, J. 1975 *Mathematical Biofluiddynamics*. Society for Industrial and Applied Mathematics.

Miloh, T. & Galper, A. 1993 Self-propulsion of general deformable shapes in a perfect fluid. *Proc. R. Soc. Lond.* A **442**, 273–299.

Montgomery, R. 1990 Isoholonomic problems and some applications. *Commun. Math. Phys.* **128**, 565–592.

Moran, J. 1984 *An Introduction to Theoretical and Computational Aerodynamics*. John Wiley & Sons.

Peskin, C. S. 2002 The immersed boundary method. *Acta Numerica* **11**, 479–517.

Purcell, E. M. 1977 Life at low Reynolds number. *Am. J. Phys.* **45** (1), 3–11.

Radford, J. 2003 Symmetry, reduction and swimming in a perfect fluid. PhD thesis, California Institute of Technology.

Saffman, P. G. 1992 *Vortex Dynamics*. Cambridge Monographs on Mechanics and Applied Mathematics.

Sfakiotakis, M., Lane, D. M. & Davies, J. B. C. 1999 Review of fish swimming modes for aquatic locomotion. *IEEE J. Oceanic Engng* **24** (2), 237–252.

Shapere, A. & Wilczek, F. 1987 Self-propulsion at low Reynolds number. *Phys. Rev. Lett.* **58** (2), 2051–2054.

Shashikanth, B. N. 2006 Symmetric pairs of point vortices interacting with a neutrally buoyant two-dimensional circular cylinder. *Phys. Fluids* **18**, 127103.

Shashikanth, B. N., Marsden, J. E., Burdick, J. W. & Kelly, S. D. 2002 The Hamiltonian structure of a two-dimensional rigid circular cylinder interacting dynamically with *N* Point vortices. *Phys. Fluids* **14** (3), 1214–1227 (see also Erratum *Phys. Fluids* **14** (11), 4099).

Shashikanth, B. N., Sheshmani, A., Kelly, S. D. & Marsden, J. E. 2008 Hamiltonian structure for a neutrally buoyant rigid body interacting with *N* vortex rings of arbitrary shape: the case of arbitrary smooth body shape. *Theor. Comput. Fluid Dyn.* **22**, 37–64.

Shukla, R. K. & Eldredge, J. E. 2007 An inviscid model for vortex shedding from a deforming body. *Theor. Comput. Fluid Dyn.* **21** (5), 343–368.

Tam, D. & Hosoi, A. E. 2007 Optimal stroke patterns for Purcell's three-link swimmer. *Phys. Rev. Lett.* **98**, 068105.

Tytell, E. D. 2004 The hydrodynamics of eel swimming: II. Effect of swimming speed. *J. Exp. Biol.* **207**, 3265–3279.

Tytell, E. D. & Lauder, G. V. 2004 The hydrodynamics of eel swimming: I. Wake structure. *J. Exp. Biol.* **207**, 1825–1841.

Weihs, D. 1972 A hydrodynamical analysis of fish turning manoeuvres. *Proc. R. Soc. Lond.* B **182**, 59–72.

Weihs, D. 1973 The mechanism of rapid starting of slender fish. *Biorheology* **10**, 343–350.

Wu, T. 1961 Swimming of a waving plate. *J. Fluid Mech.* **10**, 321–344.

Wu, T. 1971*a* Hydrodynamics of swimming propulsion. Part 1. Swimming of a two-dimensional flexible plate at variable forward speeds in an inviscid fluid. *J. Fluid Mech.* **46** (2), 337–355.

Wu, T. 1971*b* Hydrodynamics of swimming propulsion. Part 2. Some optimum shape problems. *J. Fluid Mech.* **46** (3), 521–544.

Zhu, Q., Wolfgang, M. J., Yue, D. K. P. & Triantafyllou, M. S. 2002 Three-dimensional flow structures and vorticity control in fish-like swimming. *J. Fluid Mech.* **468**, 1–28.